The elusive active nucleus of NGC 4945

Marconi, A.; Oliva, E.; Werf, P.P. van der; Maiolino, R.; Schreier, E.J.; Macchetto, F.; Moorwood, A.F.M.

Astron. Astrophys. 357, 24–36 (2000)

ASTRONOMY AND ASTROPHYSICS

The elusive active nucleus of NGC 4945⋆

A. Marconi[1], **E. Oliva**[1], **P.P. van der Werf**[2], **R. Maiolino**[1], **E.J. Schreier**[3], **F. Macchetto**[3,4], **and A.F.M. Moorwood**[5]

[1] Osservatorio Astrofisico di Arcetri, Largo E. Fermi 5, 50125 Firenze, Italy
[2] Sterrewacht Leiden, P.O. Box 9513, 2300 RA Leiden, The Netherlands
[3] Space Telescope Science Institute, 3700 San Martin Drive, Baltimore, MD 21218, USA
[4] Affiliated to ESA science division
[5] European Southern Observatory, Karl-Schwarzschild-Strasse 2, 85748 Garching bei München, Germany

Received 27 July 1999 / Accepted 4 February 2000

Abstract. We present new HST NICMOS observations of NGC 4945, a starburst galaxy hosting a highly obscured active nucleus that is one of the brightest extragalactic sources at 100 keV. The HST data are complemented with ground based [Fe II] line and mid-IR observations.

A 100pc-scale starburst ring is detected in Paα, while H_2 traces the walls of a super bubble opened by supernova-driven winds. The conically shaped cavity is particularly prominent in Paα equivalent width and in the Paα/H_2 ratio. Continuum images are heavily affected by dust extinction and the nucleus of the galaxy is located in a highly reddened region with an elongated, disk-like morphology. No manifestation of the active nucleus is found, neither a strong point source nor dilution in CO stellar features, which are expected tracers of AGN activity.

Even if no AGN traces are detected in the near-IR, with the currently available data it is still not possible to establish whether the bolometric luminosity of the object is powered by the AGN or by the starburst: we demonstrate that the two scenarios constitute equally viable alternatives. However, the absence of any signature other than in the hard X-rays implies that, in both scenarios, the AGN is non-standard: if it dominates, it must be obscured in all directions, conversely, if the starburst dominates, the AGN must lack UV photons with respect to X-rays.

An important conclusion is that powerful AGNs can be hidden even at mid-infrared wavelengths and, therefore, the nature of luminous dusty galaxies cannot be always characterized by long-wavelength data alone but must be complemented with sensitive hard X-ray observations.

Key words: galaxies: active – galaxies: individual: NGC 4945 – galaxies: nuclei – galaxies: Seyfert – galaxies: starburst – infrared: galaxies

Send offprint requests to: A. Marconi

⋆ Based on observations made with the NASA/ESA Hubble Space Telescope, obtained at the Space Telescope Science Institute, which is operated by AURA, Inc., under NASA contract NAS 5-26555. Also based on observation collected at European Southern Observatory, La Silla, Chile.

1. Introduction

A key problem in studies of objects emitting most of their energy in the FIR/submm is to establish the relative importance of highly obscured Active Galactic Nuclei (AGN) and starburst activity. In particular, it is important to know if it is still possible to hide an AGN, contributing significantly to the bolometric emission, when optical to mid-IR spectroscopy and imaging reveal only a starburst component.

Several pieces of evidence suggest that most cosmic AGN activity is obscured. Most, and possibly all, cores of large galaxies host a supermassive black hole (10^6–$10^9 M_\odot$; e.g. Richstone et al. 1998). To complete the formation process in a Hubble time, accretion must proceed at high rates, producing quasar luminosities ($L \sim 10^{12} L_\odot$). However the observed black hole density is an order of magnitude greater than that expected from the observed quasar light, assuming accretion efficiency of 10%, suggesting that most of the accretion history is obscured (e.g. Fabian & Iwasawa 1999, and references therein). It is estimated either that 85% of all AGNs are obscured (type 2) or that 85% of the accretion history of an object is hidden from view.

In addition, the hard X-ray background (> 1 keV) requires a large population of obscured AGNs at higher redshifts ($z \sim 1$) since the observed spectral energy distribution cannot be explained with the continua of Quasars, i.e. un-obscured (type 1) AGNs (Comastri et al. 1995; Gilli et al. 1999). Despite the above evidence, detections of obscured AGNs at cosmological distances are still sparse (e.g. Akiyama et al. 1999).

Ultra Luminous Infrared Galaxies (ULIRGs; see Sanders & Mirabel 1996 for a review) and the sources detected in recent far-infrared and submm surveys performed with ISO and SCUBA (e.g. Rowan-Robinson et al. 1997; Blain et al. 1999 and references therein) are candidate to host the missing population of type 2 AGNs. However, mid-IR ISO spectroscopy has recently shown that ULIRGs are mostly powered by starbursts and that no trace of AGNs is found in the majority of cases (Genzel et al. 1998; Lutz et al. 1998). Yet, the emission of a hidden AGN could be heavily absorbed even in the mid-IR. Indeed, the obscuration of the AGN could be related to the starburst phenomenon, as observed for Seyfert 2s (Maiolino et al. 1995). Fabian et al. (1998) proposed that the energy input

from supernovae and stellar winds prevents interstellar clouds from collapsing into a thin disk, thus maintaining them in orbits that intercept the majority of the lines of sight from an active nucleus.

In this paper, we investigate the existence of completely obscured AGNs and the Starburst-AGN connection through observations of NGC 4945, one of the closest galaxies where an AGN and starburst coexist. NGC 4945 is an edge-on ($i \sim 80°$), nearby ($D = 3.7\,\mathrm{Mpc}$) SB spiral galaxy hosting a powerful nuclear starburst (Koornneef 1993; Moorwood & Oliva 1994a). It is a member of the Centaurus group and, like the more famous Centaurus A (NGC 5128), its optical image is marked by dust extinction in the nuclear regions. The ONLY evidence for a hidden AGN comes from the hard X-rays where NGC 4945 is characterized by a Compton-thick spectrum (with an absorbing column density of $N_{\rm H} = 5 \times 10^{24}\,\mathrm{cm}^{-2}$, Iwasawa et al. 1993) and one of the brightest 100 keV emissions among extragalactic sources (Done et al. 1996). Recently, BeppoSAX clearly detected variability in the 13-200 keV band (Guainazzi et al. 2000).

Its total infrared luminosity derived from IRAS data is $\sim 2.4 \times 10^{10} \mathrm{L}_\odot$ (Rice et al. 1988), $\sim 75\%$ of which arises from a region of $\leq 12'' \times 9''$ centered on the nucleus (Brock et al. 1988). Although its star formation and supernova rates are moderate, $\sim 0.4\,\mathrm{M}_\odot\,\mathrm{yr}^{-1}$ and $\sim 0.05\,\mathrm{yr}^{-1}$ (Moorwood & Oliva 1994a), the starburst activity is concentrated in the central $\sim 100\,\mathrm{pc}$ and has spectacular consequences on the circumnuclear region which is characterized by a conical cavity evacuated by a supernova-driven wind (Moorwood et al. 1996a).

The radio emission is characterized by a compact non-thermal core with a luminosity of $\simeq 8 \times 10^{38}\,\mathrm{erg\,s}^{-1}$ (Elmouttie et al. 1997). It is one of the first H_2O and OH megamaser sources detected (dos Santos & Lepine 1979; Baan 1985) and the H_2O maser was mapped by Greenhill et al. (1997) who found the emission linearly distributed along the position angle of the galactic disk and with a velocity pattern suggesting the presence of a $\sim 10^6 \mathrm{M}_\odot$ black hole. Mauersberger et al. (1996) mapped the $J = 3-2$ line of ^{12}CO which is mostly concentrated within the nuclear $\sim 200\,\mathrm{pc}$.

We present new line and continuum images obtained with the *Near Infrared Camera and Multi Object Spectrograph* (NICMOS) on-board the Hubble Space Telescope (HST), aimed at detecting AGN activity in the near-infrared. These observations are complemented by recent ground based near- and mid-IR observations obtained at the European Southern Observatory. Sect. 2 describes the observations and data reduction techniques. Results are presented in Sect. 3 and discussed in Sect. 4. Finally, conclusions will be drawn in Sect. 5. Throughout the paper we assume a distance of 3.7 Mpc (Mauersberger et al. 1996), whence $1''$ corresponds to $\simeq 18\,\mathrm{pc}$.

2. Observations and data reduction

The nuclear region of NGC 4945 was observed on March 17^{th} and 25^{th}, 1998, with NICMOS Camera 2 (MacKenty et al. 1997) using narrow and broad band filters for imaging in lines and continuum. HST observations are logged in Table 1. All observations were carried out with a MULTIACCUM sequence (MacKenty et al. 1997) and the detector was read out non-destructively several times during each integration to remove cosmic rays hits and correct saturated pixels. For each filter we obtained several exposures with the object shifted by $\sim 1''$ on the detector to remove bad pixels. The observations in the F222M and F237M filters were also repeated on a blank sky area several arcminutes away from the source to remove thermal background emission. For narrow band images, we obtained subsequent exposures in line and near continuum filters with the object at several positions on the detector.

Table 1. Log of HST observations.

Dataset	Filter	T_{exp} (sec)	Description
n4mq01010	F110W	768	J
n4mq02010	F160W	768	H
n4mq01040	F222M	288	K
n4mq01070	F237M	288	CO
n4mqa1010	F222M	288	K background
n4mqa1020	F237M	288	CO background
n4mqb1nrq	F187N	320	Paα
n4mqb1nuq	F190N	320	Paα continuum
n4mqb1o0q	F190N	320	Paα continuum
n4mqb1o3q	F187N	320	Paα
n4mqb1o9q	F187N	320	Paα
n4mqb1odq	F190N	320	Paα continuum
n4mqb1oiq	F190N	320	Paα continuum
n4mqb1olq	F187N	320	Paα
n4mqb1opq	F212N	320	H_2
n4mqb1osq	F190N	320	H_2 continuum
n4mqb1ovq	F190N	320	H_2 continuum
n4mqb1ozq	F212N	320	H_2
n4mqb1p2q	F212N	320	H_2
n4mqb1p5q	F190N	320	H_2 continuum
n4mqb1p9q	F190N	320	H_2 continuum
n4mqb1pcq	F212N	320	H_2
u29r2p01t	F606W	80	R archive
u29r2p02t	F606W	80	R archive
u2e67z01t	F606W	500	R archive

The data were re-calibrated using the pipeline software CALNICA v3.2 (Bushouse et al. 1997). A small (few percent) drift in the NICMOS bias level caused an error in the flat-fielding procedure which resulted in spurious artifacts in the final images (the so-called "pedestal problem" – Skinner et al. 1998). Given the strong signal from the galaxy, such artifacts are only visible in ratio or difference images. This effect was effectively removed using the pedestal estimation and quadrant equalization software developed by Roeland P. van der Marel which subtracts a constant bias level times the flat-field, minimizing the standard deviation in the images. For each filter, the corrected images were then aligned via cross-correlation and combined. Flux calibration of the images was achieved by multiplying the count rates ($\mathrm{adu\,s}^{-1}$) for the PHOTFLAM ($\mathrm{erg\,cm}^{-2}\,\mathrm{adu}^{-1}$) conversion factors (MacKenty et al. 1997).

Fig. 1. (following page) **a** F222M image (K band). North is up and East is left. The cross marks the location of the K nucleus and the circle represents the uncertainty on the position of the H_2O maser given by Greenhill et al. (1997). Units of the frame box are seconds of arc. The origin is at the nominal location of the H_2O maser. **b** F160W image (H). Notation as in panel **a**. **c** F110W image (J). Notation as in panel **a**. The black contours are from the H-K color image at 1.8, 2 and 2.2 levels. **d** F606W image (R band). Notation as in panel **a** except for the contours which are from the K band image. **e** H-K image. Symbols are as in **a**. **f** Truecolor (Red=F222M, Green=F110W, Blue=F606W) image.

The narrow band images obtained at wavelengths adjacent to the $\mathrm{Pa}\alpha$ and H_2 lines where used for continuum subtraction. The procedure was verified by rescaling the continuum by up to $\pm 10\%$ before subtraction and establishing that this did not significantly affect the observed emission-line structure.

WFPC2 observations in the F606W (R band) filter were retrieved from the Hubble Data Archive and re-calibrated with the standard pipeline software (Biretta et al. 1996).

Ground-based observations were obtained at the European Southern Observatory at La Silla (Chile) in the continuum L′ (3.8 μm) and N (10 μm) bands, and in the [Fe II] 1.64 μm emission line and are logged in Table 2. The L′ image was obtained with IRAC1 (Moorwood et al. 1994b) at the ESO/MPI 2.2 m telescope on May 30, 1996 using an SBRC 58×62 pixel InSb array with a pixel size of 0.″45. Double beam-switching was used, chopping the telescope secondary mirror every 0.24 s and nodding the telescope every 24 s to build up a total on-source integration time of 10 minutes in a seeing of 0.″9. The N-band image was obtained with TIMMI (Käufl et al. 1994) at the ESO 3.6m telescope on May 27, 1996 using a 64×64 Si:Ga array with 0.″46 pixels. Again using double beam switching, total on-source integration time was 40 minutes in 1″ seeing. The [Fe II] 1.64 μm image was taken with with the IRAC2B camera (Moorwood et al. 1992) on the ESO/MPI 2.2m telescope on April 1, 1998, using a 256×256 Rockwell NICMOS3 HgCdTe array with 0.″51 pixels. The [Fe II] line was scanned with a $\lambda/\Delta\lambda = 1500$ Fabry-Perot etalon covering three independent wavelength settings on the line and two on the continuum on either side of the line, for a total integration times of 24 minutes on the line in 0.″9 seeing. Standard procedures were used for sky subtraction, flat fielding, interpolation of hot and cold pixels at fixed positions on the array, recentering and averaging of the data. For the [Fe II] data, the continuum was determined from the two off-line channels and subtracted from the on-line data. The integrated [Fe II] line flux is in excellent agreement with the value determined by Moorwood & Oliva (1994a).

Table 2. Log of ground based observations.

Image	T_{exp} (min)	Date	Instrument	Telescope
L′	10	May 30, 1996	IRAC1	ESO/MPI 2.2m
N	40	May 27, 1996	TIMMI	ESO 3.6m
[Fe II]	24	April 1, 1998	IRAC2B	ESO/MPI 2.2m

Table 3. Comparison with ground based photometric data.

		Moorwood & Glass 1984		This work
Band	Ø (″)	mag	Flux[a]	Flux[a]
K	6″	9.34	7.1×10^{-15}	9.5×10^{-15}
K	18″	8.12	2.2×10^{-14}	2.5×10^{-14}
H	6″	10.7	5.7×10^{-15}	7.1×10^{-15}
H	18″	9.15	2.4×10^{-14}	2.7×10^{-14}
J	6″	12.70	2.4×10^{-15}	2.7×10^{-15}
J	18″	10.80	1.4×10^{-14}	1.6×10^{-14}

[a] In units of $\mathrm{erg\,s^{-1}\,cm^{-2}\AA^{-1}}$.
[b] The K band of ground based observations corresponds to the F222M NICMOS filter. Similarly H and J corresponds to F160W and F110W, respectively.

3. Results

3.1. Morphology

Panels a–d in Fig. 1 are the continuum images in the NICMOS K, H, J and WFPC2 R filters[1]. The cross marks the position of the K band peak and the circle is the position of the H_2O maser measured by Greenhill et al. (1997). The radius of the circle is the $\pm 1''$ r.m.s. uncertainty of the astrometry performed on the images and based on the Guide Star Catalogue (Voit et al. 1997). The position of the K peak is offset by $\sim 0.''5$ from the location of the H_2O maser, hereafter identified with the location of the nucleus of the galaxy. Note that this offset is still within the absolute astrometric uncertainties of the GSC and the K peak could be coincident with the nucleus. The continuum images are also shown with a "true color" RGB representation in Fig. 1f (Red=F222M, Green=F110W, Blue=F606W). A comparison of photometry between our data and earlier published results is not straightforward since the NICMOS filters are different from the ones commonly used. However, as shown in Table 3, our measured fluxes in 6″ and 18″ circular apertures centered on the K band peak are within 15-30% of the ones by Moorwood & Glass (1984) measured in the same areas.

Fig. 1e is the H-K color map. H-K contours are also overlayed on the J image in Fig. 1c. At the location of the maser, South-East of the K band peak, emission from galactic stars is obscured by a dust lane oriented along the major axis of the galactic disk. The morphology of this resembles an edge-on disk with a 4.″5 radius (80 pc) and probably marks the region where high density molecular material detected in CO is concentrated (e.g. Mauersberger et al. 1996). The average H-K color is ~ 1.7 with a peak value of 2.3. The dust lane has a sharp southern edge which is not very evident in the color map and can be explained by saturated absorption: background H and K emission becomes completely undetectable and the color is dominated by foreground stars. Therefore, the sharp K edge is evidence for a region with such high extinction that it is not detected even in the near-IR. With this dust distribution, the observed

[1] Color images are also available at http://www.arcetri.astro.it/∼marconi

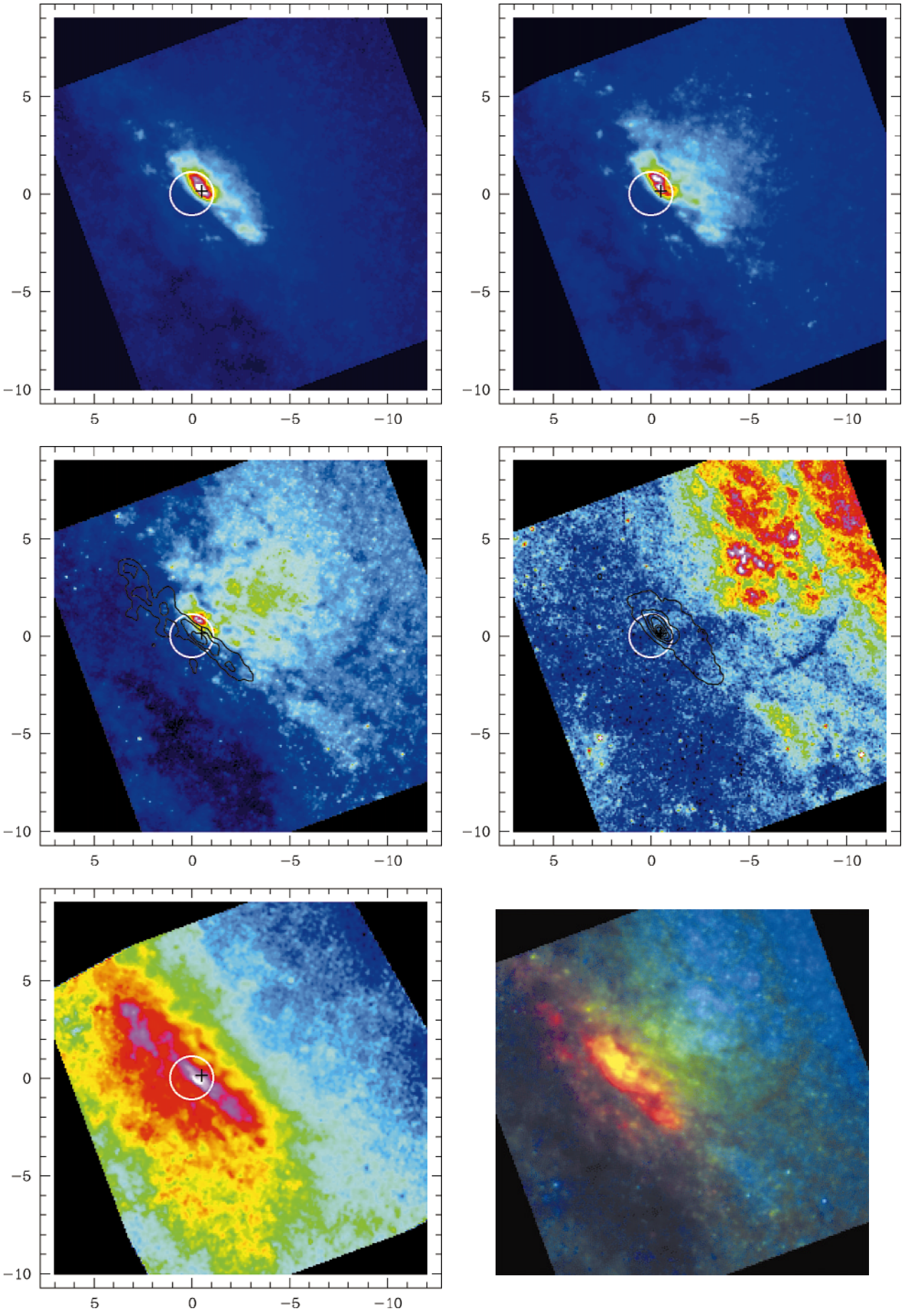
5
0
−5
−10
5
0
−5
−10

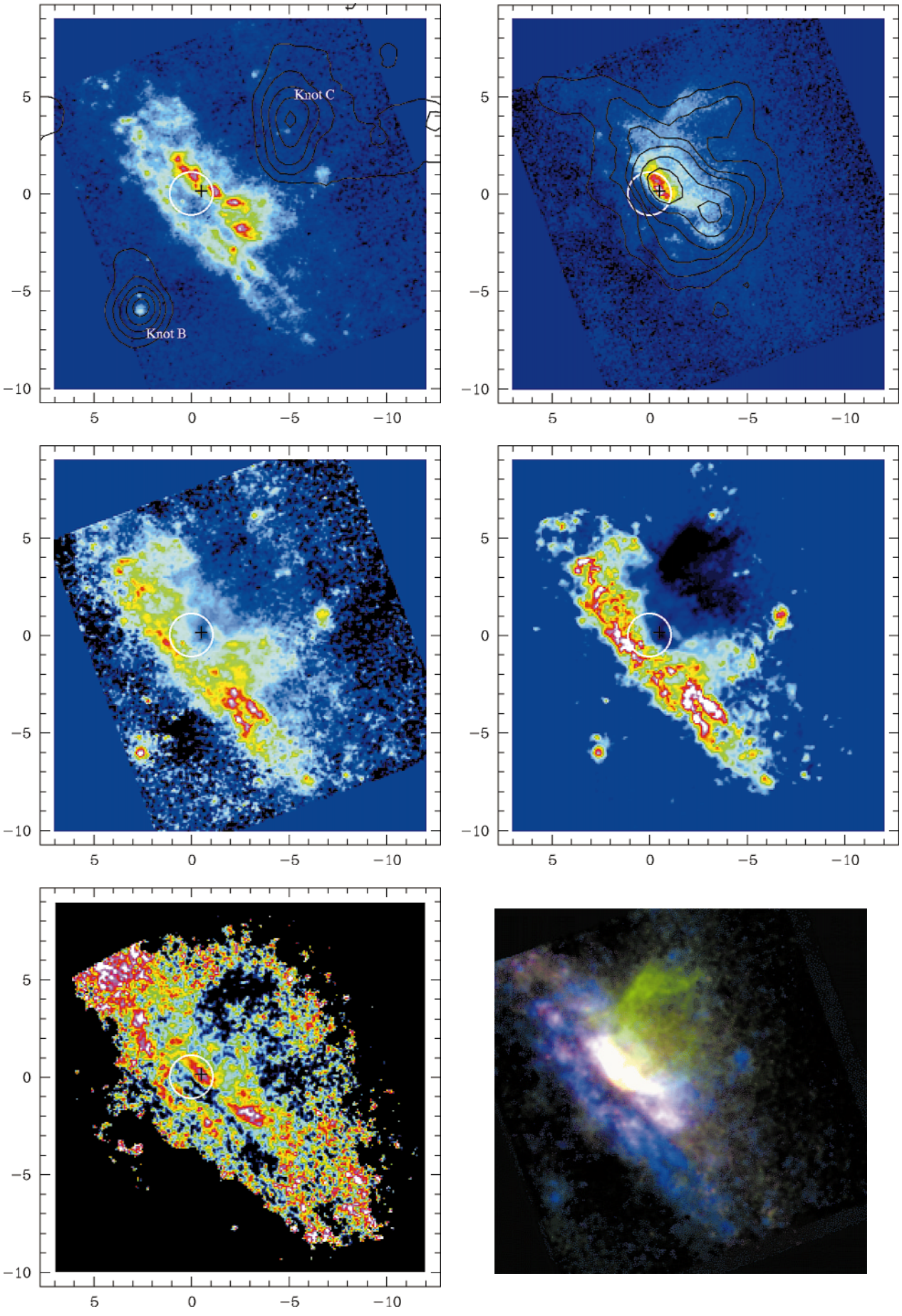
Knot C
Knot B
5
0
−5
−10

Fig. 2. (preceding page) **a** Paα image. Symbols as in Fig. 1. The black contours are from the Hα+[N II] image by Moorwood et al. (1996). **b** H_2 image. Black contours are from the blue ground-based [Fe II] image, **c** Equivalent width of Paα. **d** Paα/H_2 image. Symbols as in Fig. 1. **e** CO index. Symbols as in Fig. 1. **f** Truecolor line image (Red=F222M, Green=H_2, Blue=Paα) image.

morphology in the continuum images is the result of an extinction gradient in the direction perpendicular to the galactic disk. Patchy extinction is also present all over the field of view. At shorter wavelengths, the morphology is more irregular because dust extinction is more effective (the same effect seen so obviously in Centaurus A, cf. Schreier et al. 1998; Marconi et al. 2000) and the conical cavity extensively mapped by Moorwood et al. (1996a) becomes more prominent: there, the dust has been swept away by supernova-driven winds. Indeed, in the R image, significant emission is detected only in the wind-blown cavity which presents a clear conical morphology with well defined edges and apex lying $\simeq 3''$ from the K peak. Due to the above mentioned reddening gradient, the apex of the cone gets closer to the nucleus with increasing wavelength (compare with R band and Paα/H_2 images – see below).

The continuum-subtracted Paschen α image (Fig. 2a) shows the presence of several strong emission line knots along the galactic plane, very likely resulting from a circumnuclear ring of star formation seen almost edge-on. "Knot B" of Moorwood et al. (1996a) is clearly observed South East of the nucleus while "Knot C", North-West of the nucleus, is barely detected. Both knots are also marked on the figure.

Dust extinction strongly affects the Paα morphology making very difficult to trace the ring and locate its center; a likely consequence is the apparent misalignment between the galaxy nucleus and the ring center. The observed ring of star formation is similar to what has been found in other starburst galaxies (cf. Moorwood 1996b). The starburst ring could result from two alternative scenarios: either the starburst originates at the nucleus, and then propagates outward forming a ring in the galactic disk; or the ring corresponds to the position of the inner Lindblad resonance where the gas density is naturally increased by flow from both sides (see the review in Moorwood 1996b).

Panel b shows the continuum-subtracted H_2 image which traces the edges of the wind-blown cavity. As expected, the morphology is completely different from that of Paα which traces mainly starburst activity. Note the strong H_2 emission close to the nucleus at the apex of the cavity with an elongated, arc-like morphology. The H_2 flux in a $6'' \times 6''$ aperture centered on the K band peak is $1.1\times10^{-13}\,\mathrm{erg\,cm^{-2}\,s^{-1}}$ and corresponds to $\sim 70\%$ of the total integrated emission in the NICMOS field of view. This is in good agreement with the 1.29 ± 0.05 found by Koornneef & Israel (1996) in an equally sized aperture and the integrated $3.1\times10^{-13}\,\mathrm{erg\,cm^{-2}\,s^{-1}}$ from the map by Moorwood & Oliva (1994a). We remark that contamination of H_2 emission by He Iλ2.112 μm is unlikely since the line was detected neither by Koornneef (1993) nor by Moorwood & Oliva (1994a) and from their spectra we can set an upper limit of 5-10% to the He I/H_2 ratio.

Panel c in Fig. 2 shows that the equivalent width of Paα is up to 150–200Å in the star forming regions, but much lower in the wind-blown cavity. Since near-IR continuum emission within the cone is not significantly higher than in the surrounding medium, the low equivalent width within the cone is due to weaker Paα emission, the likely consequence of low gas density.

Panel d in Fig. 2 is the Paα/H_2 ratio image which also traces the wind-blown cavity. Note that the cone traced by Paα and H_2 is offset with respect to the light cone observed in R: this is a result of the reddening gradient in the direction perpendicular to the galactic plane.

Fig. 2f is a true color RGB representation of line and continuum images (Red=F222M, Green=H_2, Blue=Paα).

L′ and N band ground based images are shown in Fig. 3 a and b with contours overlayed on the NICMOS K band image. No obvious point source is detected at the location of the nucleus and the extended emission is smooth and regular, elongated as the galactic disk.

The [Fe II] emission shown in contours in Fig. 2b deviates from the Paα image in a number of interesting ways. First, the northern edge of the cavity outlined most clearly in H_2 emission is also detected, although more faintly, in [Fe II], presumably excited by the shocks resulting from the superwind. Otherwise, the [Fe II] emission displays two prominent peaks in the starburst region traced by Paα, one peak close to the nucleus and one offset at a position angle of about 250 degrees (counterclockwise from North). In both of these regions the [Fe II]/Paα ratio is much higher than in the rest of the starburst region. The [Fe II] emission likely originates in radiative supernova remnants (SNRs). In the dense nuclear region of NGC4945 the radiative phase of the SNRs will be short, and hence the [Fe II] emission will be much more strongly affected by the stochastic nature of supernova explosions in the starburst ring than Paα. The regions of high [Fe II]/Paα ratios thus simply trace recent supernova activity.

3.2. Reddening

A lower limit and a reasonable estimate of reddening can be obtained from the H–K color image in the case of foreground screen extinction. In this case, the extinction is simply

$$A_{\mathrm{V}} = \frac{E(H-K)}{c(H)-c(K)} \tag{1}$$

where the color excess is given by the difference between observed and intrinsic colour, $E(H-K) = (H-K)-(H-K)_\circ$ and the c coefficients represent the wavelength dependence of the extinction law; $A_\lambda = c(\lambda)A_{\mathrm{V}}$. We have assumed $A_\lambda = A_{1\,\mu\mathrm{m}}(\lambda/1\,\mu\mathrm{m})^{-1.75}$ ($\lambda > 1\,\mu$m) and $A_{\mathrm{V}} = 2.42A_{1\,\mu\mathrm{m}}$. Spiral and elliptical galaxies have average intrinsic colours $(H-K)_\circ \sim 0.22$ with 0.1 mag dispersion (Hunt et al. 1997) and the color correction due to the non-standard filters used by NICMOS is negligible – $(H-K)_\circ \sim 0.26$ instead of 0.22. In

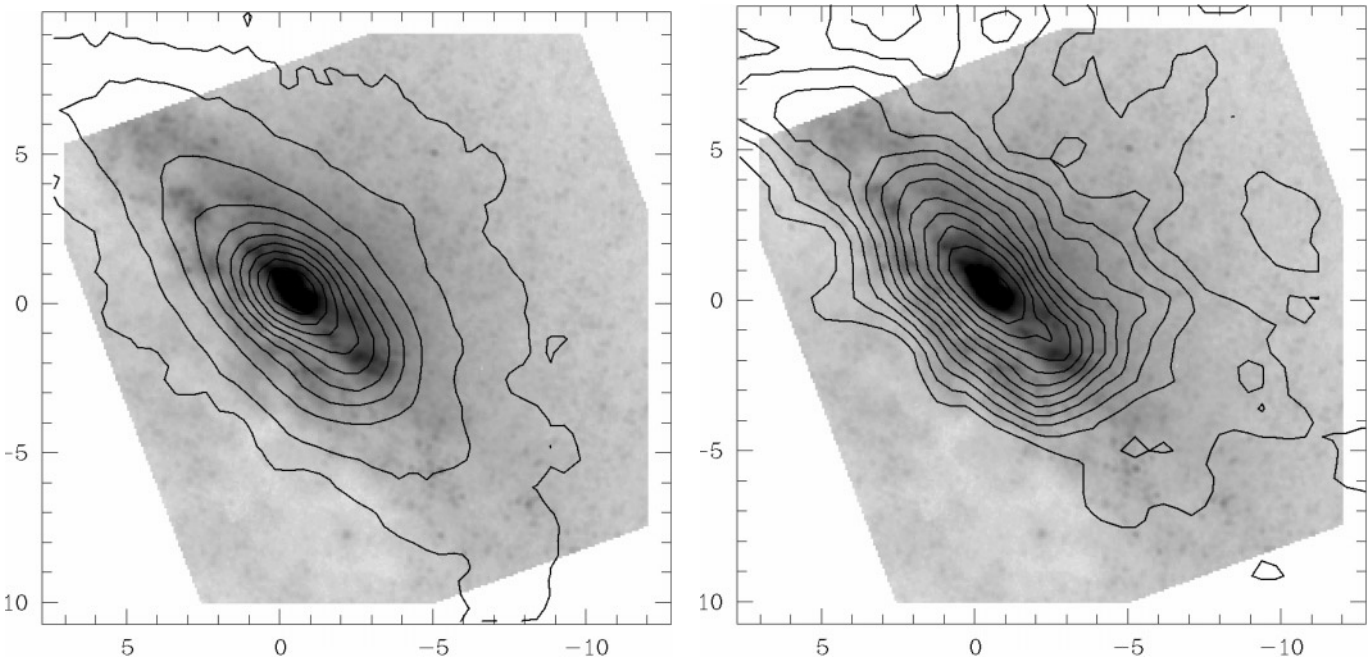

Fig. 3. **a** L band contours overlayed on the NICMOS K band image (displayed with a logarithmic look-up table). Contours are 0.005 and from 0.01 to 0.14 with step of 0.01 (units of $10^{-16}\,\mathrm{erg\,cm^{-2}\,s^{-1}\AA^{-1}}$). The frame boxes are centered on the nucleus, identified with the H_2 maser position. **b** N band contours overlayed on the NICMOS K band image. Contours are from 0.02 to 0.08 with step of 0.003 (units and notation as above).

the region of the Paα ring, the average color $H-K=1.1$ yields $A_{\rm V}\simeq 11$, in fair agreement with the estimate $A_{\rm V}>13$ from the Balmer decrement presented below. In knot B $(H-K)=1.2$ yields $A_{\rm V}=12.5$, while in knot C $(H-K)=0.64$ yields $A_{\rm V}=5.2$.

A different reddening estimate can be derived from the analysis of Hydrogen line ratios. We can estimate the reddening to "Knot B" and "Knot C" by using the images and spectra published by Moorwood et al. (1996a). The inferred reddening (assuming an intrinsic ratio Paα/Hα=0.18, and $A(\mathrm{H}\alpha)=0.81A_{\rm V}$, $A(\mathrm{Pa}\alpha)=0.137A_{\rm V}$) is $A_{\rm V}$=3.2 for Knot B and $A_{\rm V}$=3.8 for Knot C. We can also estimate a lower limit to the reddening on the Paα ring. Considering a region $\sim 11''\times 5''$ aligned along the galactic plane, including all the stronger Paα emission, we find Paα/H$\alpha>500$ which corresponds to $A_{\rm V}>13$mag, a value in agreement with the estimate given by Moorwood & Oliva (1988), $A_{\rm V}=14\pm 3$, from the Brα/Brγ ratio in a $6''\times 6''$ aperture centered on the IR peak.

We note that the first approach measures the mean extinction of the starlight, while the second one measures the extinction toward the HII regions. Therefore, these $A_{\rm V}$ estimates indicate that in the case of Knot C the star light and the emitting gas are located behind the same screen. Conversely, Knot B has a lower extinction and must therefore be located in front of the screen hiding the star light. A likely interpretation is that Knot C is located within the galactic plane on the walls of the cavity farthest from us. whereas Knot B is located above the galactic plane, toward the observer

It appears that the hypothesis of screen extinction can provide reasonable results. Of course the true extinction, i.e. the optical depth at a given wavelength, is larger if dust is mixed with the emitting regions. However, it should be noted that the case in which dust is completely and uniformly mixed with the emitting regions does not apply here because the observed color excesses are larger than the maximum value expected in that case ($E(H-K)\sim 0.6$).

3.3. CO index

A straight computation of the CO stellar index as $W(CO)=m(CO)-m(K)$, where $m(CO)$ and $m(K)$ are the magnitudes in the CO and K filters, is hindered by the high extinction gradients. Therefore we have corrected for the reddening using the prescription described above:

$$W(CO) = m(CO)-m(K) + \frac{c(K)-c(CO)}{c(H)-c(K)}E(H-K) \quad (2)$$

where, as above, the c coefficients represent the wavelength dependence of the reddening law. The correction is $0.145\,E(H-K)$ which is important since the expected CO index is ~ 0.2.

The "corrected" photometric CO index map is displayed in Fig. 2e.

As a check, in the central $4''\times 4''$ we derive a photometric CO index of 0.18 which is in good agreement with the value 0.22 obtained from spectroscopic observations by Oliva et al. (1995), when one takes into account the uncertainties of reddening correction.

In the central region there are three knots where the CO index reaches values $\simeq 0.25$ aligned along the galactic disk.

However, we do not detect any clear indication of dilution by a spatially unresolved source, that would be expected in the case of emission by hot ($\sim 1000\,\mathrm{K}$) dust heated by the AGN. There are regions close to the location of the H_2O maser where the CO index is as low as 0.08 but that value is still consistent with pure stellar emission or, more likely, with an imperfect reddening correction.

3.4. AGN activity

The NICMOS observations presented in this paper were aimed at detecting near-IR traces of AGN activity in the central ($R < 10''$) region of NGC 4945. Indeed, recent NICMOS studies exploiting the high spatial resolution of HST show that active galactic nuclei are usually characterized by prominent point sources in K, detected e.g. in the Seyfert 2 galaxies Circinus (Maiolino et al. 2000) and NGC 1068, and the radio galaxy Centaurus A (Schreier et al. 1998). NGC 4945 does not show any point-like emission at the position of the nucleus (identified by the H_2O maser) and the upper limit to the nuclear emission is $F_\lambda(\mathrm{F222M}) < 2 \times 10^{-13}\,\mathrm{erg\,cm^{-2}\,s^{-1}}\,\mu\mathrm{m}^{-1}$.

We also do not detect any dilution of the CO absorption features by hot dust emission, as observed in many active galaxies (Oliva et al. 1999b). From the analysis of the CO index image, non-stellar light contributes less than $F_\lambda(\mathrm{F222M}) < 6 \times 10^{-14}\,\mathrm{erg\,cm^{-2}\,s^{-1}}\,\mu\mathrm{m}^{-1}$ thus providing a tighter upper limit than above.

The lack of a point source in the ground based L and N observations also places upper limits on the mid-IR emission, though less tight due to the lower sensitivity and spatial resolution ($F_\lambda(\mathrm{L}) < 1.2 \times 10^{-12}\,\mathrm{erg\,cm^{-2}\,s^{-1}}\,\mu\mathrm{m}^{-1}$ and $F_\lambda(\mathrm{N}) < 6.0 \times 10^{-13}\,\mathrm{erg\,cm^{-2}\,s^{-1}}\,\mu\mathrm{m}^{-1}$).

Finally, type 2 AGNs are usually characterized by ionization cones detected either in line images or in excitation maps, i.e. ratios between high and low excitation lines (usually [O III] and Hα) revealing higher excitation than the surrounding medium. In NGC 4945 the equivalent width of Paα and the Paα/H_2 ratio indeed show a cone morphology but the behaviour is the opposite of what expected, i.e. the excitation within the cone is lower than in the surroundings and the H_2/Paα ratio increases up to ~ 5 (see Fig. 2d). Two processes could be responsible for the enhanced H_2 emission – either shocks caused by the interaction between the supernova-driven wind and the interstellar medium or exposure to a strong X-ray dominated photon flux emitted by the AGN. But in any case there is absolutely no indication of the strong UV flux which produces "standard" AGN ionization cones.

We find, therefore, no evidence for the expected AGN markers in our NICMOS data.

4. Discussion

Although no trace of its presence has been found in these data, the existence of an obscured AGN in the nucleus of NGC 4945 is unquestionably indicated by the X-rays (Iwasawa et al. 1993; Done et al. 1996). Recent, high signal-to-noise observations by BeppoSAX (Guainazzi et al. 2000) have confirmed the previous indications of variability from Ginga observations (Iwasawa et al. 1993): in the 13-200 keV band, where the transmitted spectrum is observed, the light curve shows fluctuations with an extrapolated doubling/halving time scale of $\tau \sim 3 - 5 \times 10^4\,\mathrm{s}$. These time scales and amplitudes essentially exclude any known process for producing the high energy X-rays other than accretion onto a supermassive black hole.

Making the $3\times10^{42}\,\mathrm{erg\,s^{-1}}$ observed in the 2-10 keV band with BeppoSAX would require about 10000 of the most luminous X-ray binaries observed in our Galaxy (e.g. Scorpio-X1) and only a few of this objects are known.

Alternatively, very hot plasma ($KT \sim$ a few keV), due to supernovae, has been observed in the 2-10 keV spectrum of starburst galaxies, but at higher energies ($> 30\,\mathrm{keV}$) the emission is essentially negligible (Cappi et al. 1999; Persic et al. 1998); whereas the emission of NGC4945 peaks between 30 and 100 keV. Also, given that the X-ray emission is observed through a gaseous absorbing column density of a few times $10^{24}\,\mathrm{cm^{-2}}$, both the 10000 superluminous X-ray binaries and the very hot SN wind should be hidden by this huge gaseous column. It is very difficult to find a geometry for the gas distribution that could produce this effect. We therefore conclude that the presence of an AGN provides the only plausible origin of the hard X-ray emission.

The above considerations combined with the absence of any evidence for the presence of an AGN at other wavelengths has important consequences irrespective of the relative, and unknown, contributions of the starburst and AGN to the total bolometric luminosity. This is illustrated below by considering the extreme possibilities that the luminosity is dominated either by the starburst or the AGN.

4.1. NGC 4945 as a starburst dominated object

Most previous studies have concluded that the FIR emission in NGC 4945 can be attributed solely to starburst activity (e.g. Koornneef 1993; Moorwood & Oliva 1994a) without invoking the presence of an AGN.

We note that, on average, active galaxies are characterized by $L_{FIR}/L_{Br\gamma}$ ratios much larger than starbursts and this fact was sometimes invoked to discern starbursts from AGNs (see the discussion in Genzel et al. 1998). In this regard, NGC 4945 has a starburst-like ratio: $L_{\mathrm{FIR}}/L_{\mathrm{Br}\gamma} \sim 1.4 \times 10^5$ (from observed Paα with A_V=15mag). This is similar to the value for the prototypical starburst galaxy M82 ($L_{\mathrm{FIR}}/L_{\mathrm{Br}\gamma} \sim 3.4 \times 10^5$, Rieke et al. 1980), suggesting that the FIR emission of NGC 4945 may arise from the starburst.

Genzel et al. (1998) showed that, when considering the reddening correction derived from the mid-IR – usually much larger than from the optical and near-IR – the observed H line emission from the starburst translates into an ionizing luminosity comparable to the FIR luminosity. Indeed, if in NGC 4945 the bulk of H emission is hidden by just A_V=45mag, $L_{\mathrm{FIR}}/L_{\mathrm{ion}} \sim 1$ and the observed starburst activity is entirely responsible for the FIR.

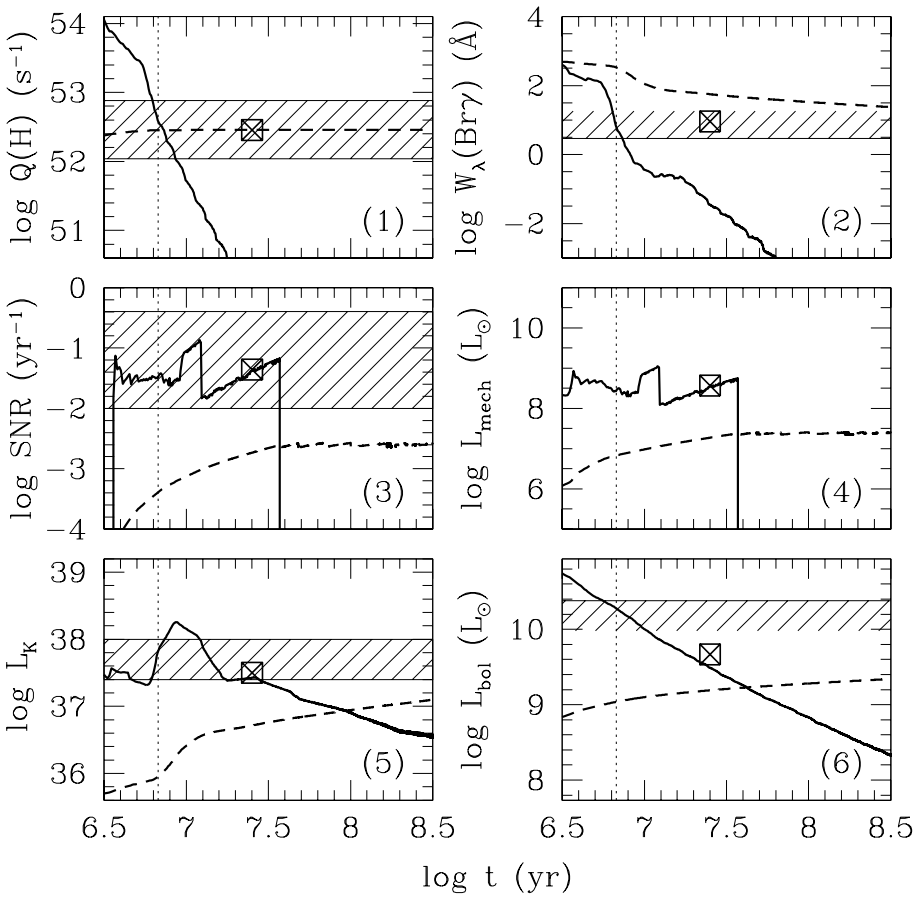

Fig. 4. Properties of a burst of star formation as a function of the time elapsed from the beginning of the burst (models by Leitherer et al. 1999). The thick solid line represents an instantaneous burst with mass $3.5\times10^7\mathrm{M}_\odot$. The thick dashed line is a continuous star formation rate of $0.13\mathrm{M}_\odot\,\mathrm{yr}^{-1}$. See text for more details on the models. Panel 1 is the time dependence of the ionizing photon rate. The shaded area limits values consistent with observations. The thin dotted line is drawn at a time in which the "instantaneous" burst meets the observational constraints. The crossed square represents the combination of the properties of the two models at $t = 10^{7.4}\,\mathrm{yr}$. Panel 2 gives the $\mathrm{Br}\gamma$ equivalent width. The shading outline the lower limit given by observations. The other symbols are as in panel 1. Panel 3 gives the Supernova Rate. As above the shaded area limits the range of values allowed from observations. Symbols as in panel 1. Panel 4 gives the mechanical luminosity. Symbols as in panel 1. Panel 5 gives the monochromatic luminosity in the K band ($\mathrm{erg\,s^{-1}}$Å). Symbols as in panel 1. Panel 6 gives the bolometric luminosity of the burst. The shading marks the upper limit set by the total IRAS luminosity of the galaxy.

Although all the bolometric luminosity could be generated by a starburst it is also possible to construct starburst models which are consistent with the observed near infrared properties but generate a much lower total luminosity. It is important to recall that $L_{\mathrm{FIR}}/L_{\mathrm{Br}\gamma}$ represents the ratio between star formation rates averaged over two different timescales, i.e. $> 10^8$yrs and $< 10^7$yrs, respectively. Therefore, this ratio strongly depends on the past star formation history. For example, objects which have not experienced star formation in the past 10^7yrs will emit little $\mathrm{Br}\gamma$, but significant FIR radiation. A more quantitative approach is presented in Fig. 4 where we compare the observed nuclear properties of NGC 4945 with synthesis models by Leitherer et al. (1999). We have considered two extreme cases of star formation history. The thick solid line in the figure represents an instantaneous burst with mass $3.5 \times 10^7\mathrm{M}_\odot$ whereas the thick dashed line is a continuous star formation rate of $0.13\mathrm{M}_\odot\,\mathrm{yr}^{-1}$. In both cases a Salpeter initial mass function (i.e. $\propto M^{-2.35}$), upper mass cutoff of $100\mathrm{M}_\odot$ and abundances $Z = \mathrm{Z}_\odot$ are chosen. Panel 1 shows the evolution of the ionizing photon rate ($Q(\mathrm{H})$) as a function of time after the beginning of the burst. The shaded region limits the values compatible with the observations; $Q(\mathrm{H})$ is estimated from the total $\mathrm{Pa}\alpha$ flux in the NICMOS images ($5.6 \times 10^{-13}\,\mathrm{erg\,s^{-1}\,cm^{-2}}$), dereddened with $A_V = 5$mag and $A_V = 20$mag and converted using case B approximation for H recombinations. Panel 2 gives the equivalent width of $\mathrm{Br}\gamma$ ($W_\lambda(\mathrm{Br}\gamma)$); the observed value outlined by the shaded area is a lower limit for the starburst models and was derived by rescaling the observed $\mathrm{Pa}\alpha$ flux and dividing by the flux observed in the same aperture with the F222M filter. Panel 3 is the evolution of the SuperNova Rate (SNR). Estimates of SNR from radio observations suggest values $> 0.3\,\mathrm{yr}^{-1}$ (Koornneef 1993), $0.2\,\mathrm{yr}^{-1}$ (Forbes & Norris 1998), down to $0.05\,\mathrm{yr}^{-1}$ (Moorwood & Oliva 1994a). The shaded region covers the 0.01-0.4 yr^{-1} range. Panel 4 is the mechanical luminosity produced by the Supernovae. Finally, panels 5 and 6 give the K-band and bolometric luminosity, respectively. The allowed range for the K monochromatic luminosity is given by the total observed flux in a $6'' \times 6''$ aperture centered on the K peak where photospheric emission from supergiants is known to dominate (Oliva et al. 1999b). The upper and lower limits represent the values obtained after dereddening by $A_V = 5$mag and $A_V = 20$mag. The upper limit to the bolometric luminosity is the *total* NGC 4945 luminosity derived from IRAS observations (Rice et al. 1988). In all cases the thin dotted line represents the time at which the properties of the instantaneous burst meet the observational constraints. The crossed square represent the combination of the two models at $t = 10^{7.4}\,\mathrm{yr}$.

It is clear from the figure that an instantaneous burst of $t \sim 10^{6.8}\,\mathrm{yr}$ is capable of meeting all the observational constraints. It reproduces the correct supernova rate and K band luminosity and its bolometric luminosity dominates the total bolometric luminosity of the galaxy. Conversely the continuous

burst fails to reproduce the SNR and K luminosity. Just considering these two models alone it is tempting to infer that the starburst powers the bolometric emission of NGC4945. However, the instantaneous and continuous SFR are two extreme and simplistic cases. More realistically the SF history is more complex since bursts have a finite and limited length or are the combination of several different events. As an example we consider the case of two bursts of star formation taking place at the same time: one instantaneous and the other continuous. Both have the same characteristics as the bursts presented above. The properties of this double burst model at $t = 10^{7.4}\,\mathrm{yr}$ are shown in the figure by the crossed squares. The choice of the time is arbitrary and any other value between $10^{7.2}\,\mathrm{yr}$ and $10^{7.5}\,\mathrm{yr}$ might do. Even in this case the starburst model meets all the observational constraints: $Q(\mathrm{H})$ is provided for by the continuous burst while SNR and K luminosity come from the instantaneous burst. The important difference with respect to the single instantaneous burst is that the bolometric luminosity of the burst is now $\lesssim 20\%$ of the total bolometric luminosity of the galaxy.

The mechanical luminosity injected by the SN in the "instantaneous" burst (which dominates also in the double burst model) is $\sim 10^{8.5}\mathrm{L}_\odot$ over $\sim 10^{7.4}\,\mathrm{yr}$. This results in a total injected energy of $\sim 10^{57}\,\mathrm{erg}$ which is more than enough to account for the observed superwind. Indeed Heckman et al. (1990) estimate an energy content of the winds blown cavity of $\sim 1.5\times10^{55}\,\mathrm{erg}$ (after rescaling for the different adopted distance of NGC 4945). Both models agree with the constraints imposed by dynamical measurements that the central mass in stars must be less than $6.6\times10^{8}\mathrm{M}_\odot$ (Koornneef 1993, after rescaling for the different assumed distances of the galaxy): the continuous SFR would require $5\times10^{9}\,\mathrm{yr}$ to produce that mass of stars.

In conclusion, two different star formation histories can reproduce the observed starburst properties but only in one case does the starburst dominate the bolometric luminosity of the galaxy. Therefore the available data do not allow any constraints on the bolometric luminosity of the starburst.

As shown in the next section, the observed $(L_{\mathrm{FIR}}/L_{\mathrm{X}})$ ratio of NGC 4945 is equal to that of a "normal" AGN in which the L_{FIR} is reprocessed UV radiation. If the L_{FIR} in NGC 4945 is actually dominated by the starburst, therefore, it is clear that the AGN must be strongly deficient in UV relative to X-rays.

In this starburst-dominant scenario for NGC4945, with the black hole mass inferred from the $\mathrm{H_2O}$ maser measurements (Greenhill et al. 1997), the AGN is emitting at $\lesssim$ 10% of its Eddington Luminosity.

4.2. NGC 4945 as an AGN dominated object

By fitting the simultaneous 0.1-200 keV spectrum from BeppoSAX, the absorption corrected luminosity in the 2-10 keV band is $L_{\mathrm{X}}(2-10\,\mathrm{keV}) = 3\times10^{42}\,\mathrm{erg\,s^{-1}}$ (Guainazzi et al. 2000). If the AGN in NGC 4945 has an intrinsic spectral energy distribution similar to a quasar, then $L_{\mathrm{X}}(2-10\,\mathrm{keV})/L_{\mathrm{bol}} \sim 0.03$ (Elvis et al. 1994) therefore $(L_{\mathrm{bol}})_{\mathrm{AGN}} \sim 10^{44}\,\mathrm{erg\,s^{-1}} = 2.6\times10^{10}\mathrm{L}_\odot$ which is the *total* far-IR luminosity of NGC 4945, measured by IRAS (Rice et al. 1988). Thus, a "normal" AGN in NGC 4945 *could* in principle power the total bolometric luminosity.

For this scenario, we compare NGC 4945 with a nearby obscured object, the Circinus galaxy, now considered an example of a "standard" Seyfert 2 galaxy (c.f. Oliva et al. 1994; Oliva et al. 1998; Maiolino et al. 1998a; Matt et al. 1999; Storchi-Bergmann et al. 1999; Curran et al. 1999). In particular, Oliva et al. (1999a) and, previously, Moorwood et al. (1996c) showed that the total energy output from the AGN required to explain the observed emission line spectrum is comparable to the total FIR luminosity, concluding that any starburst contribution to the bolometric luminosity is small ($\lesssim$ 10%). The choice of the Circinus galaxy is motivated by the similar distance (D=4 Mpc), FIR and hard X-ray luminosities as NGC 4945 ($L_{\mathrm{FIR}} \sim 1.2\times10^{10}\mathrm{L}_\odot$; Siebenmorgen et al. 1997 – $L_{\mathrm{X}}(2-10\,\mathrm{keV}) \sim 3.4-17\times10^{41}\,\mathrm{erg\,s^{-1}}$; Matt et al. 1999). Note that its $L_{\mathrm{X}}(2-10\,\mathrm{keV})/L_{\mathrm{FIR}}$ ratio ($\sim 0.01-0.05$) is consistent with the average value for quasars (Elvis et al. 1994).

The overall spectral energy distributions of NGC 4945 and Circinus are compared in Fig. 5. The "stars" represent the IRAS photometric points (except for the points with the largest wavelength which are the 150 μm measurements by Ghosh et al. 1992). In NGC 4945 the points labeled with "K", "L" and "N" are the upper limits derived from our observations, while in Circinus they represent emission from the unresolved nuclear source corrected for stellar emission (Maiolino et al. 1998a). The points labeled "100 keV" are from Done et al. (1996) (NGC 4945) and Matt et al. (1999) (Circinus). The bars between 13.6 and 54.4 eV are at a level given by $\nu L_\nu \sim Q(\mathrm{H})\,\langle h\nu\rangle$, where $Q(\mathrm{H})$ is the rate of H-ionizing photons and $\langle h\nu\rangle$ is the mean photon energy of the ionizing spectrum. For NGC 4945, $Q(\mathrm{H})$ is derived from H recombination lines and thus represent the energy which is radiated by the young starburst; we assumed $\langle h\nu\rangle = 16\,\mathrm{ev}$. For Circinus, the point labeled with "Starburst" is similarly derived from Brγ emission associated with the starburst (Oliva et al. 1994) while that labeled "AGN" is from the estimate made by Oliva et al. (1999a).

In the lower panel, we represent the IR spectrum of Circinus by connecting the photometric points just described. We plot this same spectrum as a dotted line in the upper panel, rescaling to match the 100 keV points. NGC 4945 and Circinus have similar X/FIR ratios: $\nu L_\nu(100keV)/L_{FIR} \simeq 2\times10^{-3}$ for Circinus and $\simeq 3\times10^{-3}$ for NGC 4945. Note that, at each wavelength, both Circinus and NGC 4945 were observed with comparable resolution.

If the AGN in NGC 4945 dominates the luminosity and its intrinsic spectrum is similar to that of Circinus, then the lack of AGN detections in the near-IR and mid-IR require larger obscuration. In particular the non-detection of a K band point source or of dilution of the CO features can be used to estimate the extinction at 2.2 μm. In Circinus from Maiolino et al. (1998a) (K band) and Matt et al. (1999), we can derive $\nu L_\nu(K)/\nu L_\nu(100keV) \simeq 0.5$. If NGC 4945 has a similar near-IR over hard-X-rays ratio then, given $\nu L_\nu(K)/\nu L_\nu(100keV) < 8\times10^{-4}$ (K band upper limit from CO and X-ray data from Done et al. 1996), the extinction toward the nucleus is $\Delta\mathrm{A_K} > 7$mag (i.e. $\Delta A_{\mathrm{V}} > 70$mag)

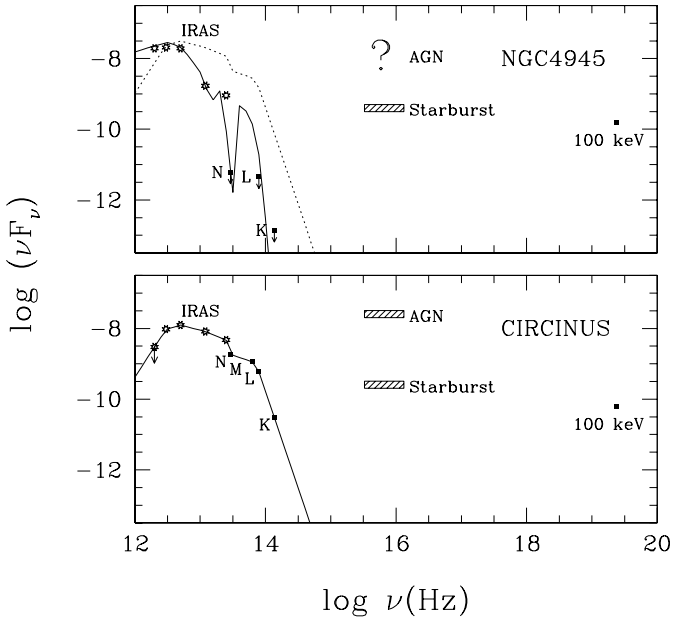

Fig. 5. Spectral energy distributions of NGC 4945 (upper panel) and Circinus (lower panel). "Stars" are the IRAS photometric points (except for the points with the highest wavelength which are from baloon-borne observations). "K", "L", "M" and "N" are the points in the standard photometric bands. The hatched areas labeled as "Starburst" and "AGN" represent the continuum levels derived from the ionizing photon rates (see text) emitted by starburst and AGN, respectively. The "100 keV" points are from X-ray observations. The IR spectrum of Circinus (solid line in lower panel) is plotted in the upper panel (dotted line) after rescaling to match the 100 keV points. The solid line in the upper panel is the same spectrum after extinction by an extra $A_{\rm V} = 150\,{\rm mag}$ (see text for details).

larger than in the case of Circinus. Hot dust in NGC 4945 must be hidden by at least $A_{\rm V} > 135\,{\rm mag}$, in agreement with the estimate by Moorwood & Glass (1984), $A_{\rm V} > 70$ and, more recently, with an analysis of ISO CVF spectra implying $A_{\rm V} \sim 100\,{\rm mag}$ (Maiolino et al., paper in preparation). We note that the required extinction is not unexpected and in agreement with the X-ray measurements. The measured column density in absorption in the X-rays is $N_{\rm H} \sim {\rm few} \times 10^{24}\,{\rm cm}^{-2}$ therefore the expected A_V, assuming a galactic gas-to-dust ratio is:

$$A_V \sim 450 \left(\frac{N_{\rm H}}{10^{24}\,{\rm cm}^{-2}} \right). \qquad (3)$$

The A_V measured from optical/IR data is estimated smaller than derived from X-rays ($A_V({\rm IR}) \sim 0.1 - 0.5\,A_V({\rm X})$; Granato et al. 1997), therefore the X-ray absorbing column density is in excellent agreement with the required extinction. Very high extinction, expected in the frame of the unified AGN model are observed in many objects as discussed and summarized, for instance, in Maiolino et al. (1998b) and in Risaliti et al. (1999).

The higher extinction can also qualitatively explain the redder colors of the NGC 4945 FIR spectrum. The solid line in the upper panel is the spectrum of Circinus after applying foreground extinction by $A_{\rm V} = 150\,{\rm mag}$. We have applied the extinction law by Draine & Lee (1984) and the energy lost in the mid-IR has been reprocessed as 40 K dust emission (i.e. black body emission at 40 K corrected for $\lambda^{-1.75}$ emissivity). Though a careful treatment requires a full radiation transfer calculation, this simple plot demonstrates that (i) the redder color of NGC 4945 with respect to Circinus can be explained with extra absorption and (ii) that this is not energetically incompatible with the observed FIR luminosity, i.e. the absorbed mid-IR emission re-radiated in the FIR does not exceed the observed points.

If the FIR emission is powered by the AGN this is UV radiation re-processed by dust. However, if the AGN emits $\sim 2 \times 10^{10} {\rm L}_\odot$ in UV photons, high excitation gas emission lines should also be observed. The absence of high ionization lines like $[{\rm O\,III}]\lambda 5007, 4959$Å (Moorwood et al. 1996a) or $[{\rm Ne\,V}]\lambda 14.3\,\mu{\rm m}$ (Genzel et al. 1998) and the low excitation observed in the wind-blown cone strongly argues that no ionizing UV photons (i.e. $13.6 \leq {\rm h}\nu < 500\,{\rm ev}$) escape from the inner region. The low excitation H_2/Paα map, associated with the peak in H_2 emission close to the nucleus location, indicates that ALL ultraviolet photons must be absorbed within $R < 1\farcs5$, i.e. $R < 30\,{\rm pc}$ along ALL lines of sight. This is in contrast with the standard unified model of AGN where ionizing radiation escapes along directions close to the torus axis.

If the AGN is embedded in a thick dusty medium then two effects will contribute to its obscuration. First, dust will compete with the gas in absorbing UV photons which will be directly converted into infrared radiation (e.g. Netzer & Laor 1993; Oliva et al. 1999a). Second, emission lines originating in this medium will be suppressed by dust absorption. To estimate the amount of required extinction, note that in Circinus $[{\rm Ne\,V}]14.3\,\mu{\rm m}/[{\rm Ne\,II}]12.8\,\mu{\rm m} = 0.4$ (extinction corrected) and in NGC 4945 $[{\rm Ne\,V}]/[{\rm Ne\,II}] \leq 0.008$ (both ratios are from Genzel et al. 1998). If NGC4945 has the same intrinsic ratio as Circinus, then the observed $[{\rm Ne\,V}]/[{\rm Ne\,II}]$ ratio requires $A(14.3\,\mu{\rm m}) > 4.2$mag corresponding to $A_{\rm V} > 110$mag and in agreement with the above estimates.

We conclude that the AGN can power the FIR emission if it is properly obscured. Inferring the black hole mass from the H_2O maser observations ($1.4 \times 10^6 {\rm M}_\odot$, Greenhill et al. 1997), we find in this scenario that the AGN is emitting at $\sim 50\%$ of its Eddington Luminosity.

4.3. On the existence of completely hidden active galactic nuclei

As discussed above, if an AGN powers the FIR emission of NGC 4945, it must be hidden up to mid-IR wavelengths and does not fit in the standard unified model. The possible existence of such a class of Active Nuclei, detectable only at $> 10\,{\rm keV}$, would have important consequences on the interpretation of IR luminous objects whose power source is still debated.

Genzel et al. (1998) and Lutz et al. (1998) compared mid-IR spectra of Ultra Luminous IRAS galaxies (ULIRGs, see Sanders & Mirabel 1996 for a review) with those of AGN and starburst templates. They concluded that the absence of high excitation lines (e.g. $[{\rm Ne\,V}]$) and the presence of PAH features undiluted by strong thermal continuum in ULIRGs spectra strongly suggest

that the starburst component is dominant. They also show that, after a proper extinction correction, the observed star formation activity can power FIR emission. In their papers, NGC 4945 is classified as a starburst because of its mid-IR properties but, as shown in the previous section, NGC 4945 could also be powered by a highly obscured AGN and the same scenario could in principle apply to all ULIRGs. Their bolometric emission can be powered by an active nucleus completely obscured even at mid-IR wavelengths.

The same argument could be used for the sources detected at submillimeter wavelengths by SCUBA which can be considered as the high redshift counterpart of local ULIRGs. If they are powered by hidden active nuclei then their enormous FIR emission would not require star formation rates in excess of $> 100 \mathrm{M}_{\odot}\,\mathrm{yr}^{-1}$ (e.g. Hughes et al. 1998), and this would have important consequences for understanding the history of star formation in high redshift galaxies.

In addition, it is well known that in order to explain the X-ray background a large fraction of obscured AGN is required. However Gilli et al. (1999) have shown that, in order to reconcile the observed X-ray background with hard X-ray counts, a rapidly evolving population of hard X-ray sources is required up to redshift ~ 1.5. No such population is known at the moment and the only class of objects which are known to undergo such a rapid density evolution are local ULIRGs (Kim et al. 1998) and, at higher redshift, the SCUBA sources (Smail et al. 1997). SCUBA sources are therefore candidates to host a population of highly obscured AGNs.

Almaini et al. (1999) suggest that, if the SED of high redshift AGN is similar to those observed locally, one can explain 10–20% of the $850\,\mu\mathrm{m}$ SCUBA sources at 1 mJy. This fraction could be significantly higher if a large population of AGN are Compton thick at X-ray wavelengths. Trentham et al. (1999) show that if the SCUBA sources are completely powered by a dust enshrouded AGN then they may help in explaining the discrepancy between the local density in super massive black holes and the high redshift AGN component (see also Fabian & Iwasawa 1999).

Establishing the nature of SCUBA sources could be extremely difficult if the embedded AGNs are like NGC4945, i.e. completely obscured in all directions, because they would then not be identifiable with the standard optical/IR diagnostics. Incidentally, this fact could possibly account for the sparse detections of type 2 AGNs at high redshifts (Akiyama et al. 1999).

The best possibility for the detection of NGC4945-like AGNs is via their hard X-ray emission but, unfortunately, the sensitivity of existing X-ray surveys is still not high enough to detect high z AGN and the low spatial resolution makes identifications uncertain in the case of faint optical/near-IR counterparts. Moreover, hard X-rays alone are not enough to establish if the AGN dominates the bolometric emission.

5. Conclusions

Our new HST NICMOS observations of NGC 4945, complemented by new ground based near and mid-IR observations, have provided detailed morphology of the nuclear region. In $\mathrm{Pa}\alpha$, we detect a 100pc-scale starburst ring while in H_2 we trace the walls of a conical cavity blown by supernova driven winds. The continuum images are strongly affected by dust extinction but show that even at HST resolution and sensitivity, the nucleus is completely obscured by a dust lane with an elongated, disk-like morphology. We detect neither a strong point source nor dilution in CO stellar features, expected signs of AGN activity.

Whereas all the infrared properties of NGC 4945 are consistent with starburst activity, its strong and variable hard X-ray emission cannot be plausibly accounted for without the presence also of an AGN. Although the starburst must contribute to the total bolometric luminosity we have shown, using starburst models, that the actual amount is dependent on the star formation history. A major contribution from the AGN is thus not excluded. Irrespective of the assumption made, however, our most important conclusion is that the observed variable hard X-ray emission combined with the lack of evidence for reprocessed UV radiation in the infrared is incompatible with the "standard" AGN model. If the AGN dominates the bolometric luminosity, then its UV radiation must be totally obscured along all lines of sight. If the starburst dominates then the AGN must be highly deficient in its UV relative to X-ray emission. The former case clearly raises the possibility that a larger fraction of ULIRGs than currently thought could actually be AGN rather than starburst powered.

Acknowledgements. A.M. and A.R. acknowledge the partial support of the Italian Space Agency (ASI) through grants ARS-98-116/22 and ARS-99-44 and of the Italian Ministry for University and Research (MURST) under grant Cofin98-02-32. E.J.S. acknowledge support from STScI GO grant O0113.GO-7865. We thank Roeland P. van der Marel for the use of the pedestal estimation and quadrant equalization software.

References

Akiyama M., Ohta K., Yamada T., et al., 1999, Proceeding of the first XMM workshop: Science with XMM. in press (astro-ph/9811012)
Almaini O., Lawrence A., Boyle B.J., 1999, MNRAS 305, L59
Baan W.A., 1985, Nat 315, 26
Biretta J.A., Burrows C., Holtzman J., et al., 1996, WFPC2 Instrument Handbook. Version 4.0, STScI, Baltimore
Blain A.W., Kneib J.P., Ivison R.J., Smail I., 1999, ApJ 512, L87
Brock D., 1988, ApJ 329, 208
Bushouse H., Skinner C.J., MacKenty J.W., 1997, NICMOS Instrument Sci. Rept. 97-28, STScI, Baltimore
Cappi M., Persic M., Bassani L., et al., 1999, A&A 350, 777
Comastri A., Setti G., Zamorani G., Hasinger G., 1995, A&A 296, 1
Curran S.J., Rydbeck G., Johansson L.E.B., Booth R.S., 1999, A&A 344, 767
Done C., Madejski G.M., Smith D.A., 1996, ApJ 463, L63
dos Santos P.M., Lepine J.R.D., 1979, Nat 278, 34
Draine B.T., Lee H.M., 1984 ApJ 285, 89
Elmouttie M., Haynes R.F., Jones K.L., et al., 1997, MNRAS 284, 830
Elvis M., Wilkes B.J., McDowell J.C., et al., 1994, ApJS 95, 1
Fabian A.C., Barcons X., Almaini O., Iwasawa K., 1998, MNRAS 297, L11

Fabian A.C., Iwasawa K., 1999, MNRAS 303, L34
Forbes D.A, Norris R.P., 1998, MNRAS 300, 757
Genzel R., Lutz D., Sturm E., et al., 1998, ApJ 498, 579
Ghosh S.K., Bisht R.S., Iyengar K.V.K., et al., 1992, ApJ 391, 111
Gilli R., Risaliti R., Salvati M., 1999, A&A 347, 424
Granato G.L., Danese L., Franceschini A., 1997, ApJ 486, 14
Greenhill L.J., Moran J.M., Herrnstein J.R., 1997, ApJ 481, L23
Guainazzi M., Matt G., Brandt W.N., et al., 2000, A&A, in press (astro-ph/0001528)
Heckman T.M., Armus L., Miley G.K., 1990, ApJS 74, 833
Hughes D.H., Serjeant S., Dunlop J., et al., 1998, Nat 394, 241
Hunt L.K., Malkan M.A., Salvati M., et al., 1997 ApJS 108, 229
Iwasawa K., Koyama K., Awaki H., et al., 1993, ApJ 409, 155
Käufl H.U., Jouan R., Lagage P.O., et al., 1994, Infrared Phys. Technol. 35, 203
Kim D.-C., Sanders D.B., 1998, ApJS 119, 41
Koornneef J., 1993, ApJ 403, 581
Koornneef J., Israel F.P., 1996, New Astronomy 1, 271
Leitherer C., Schaerer D., Goldader J.D., et al., 1999, ApJS 123, 3
Lutz D., Spoon H.W.W., Rigopoulou D., Moorwood A.F.M., Genzel R., 1998, ApJ 505, L103
MacKenty J.W., Skinner C., Calzetti D., Axon D.J., et al., 1997, NICMOS Instrument Handbook. Version 2.0, STScI, Baltimore
Maiolino R., Ruiz M., Rieke G.H., Keller L.D., 1995, ApJ 446, 561
Maiolino R., Krabbe A., Thatte N., Genzel R., 1998a, ApJ 493, 650
Maiolino R., Salvati M., Bassani L., et al., 1998b, A&A 338, 781
Maiolino R., Alonso-Herrero A., Anders S., et al., 2000, ApJ 531, 219–NB
Marconi A., Schreier E.J., Koekemoer A., et al., 2000, ApJ 528, 276
Matt G., Guainazzi M., Maiolino R., et al., 1999, A&A 341, L39
Mauersberger R., Henkel C., Whiteoak J.B., et al., 1996, A&A 309, 705
Moorwood A.F.M., Glass I.S., 1984, A&A 135, 281
Moorwood A.F.M., Oliva E., 1988, A&A 203, 278
Moorwood A.F.M., Finger G., Biereichel P., et al., 1992, The Messenger 69, 61
Moorwood A.F.M., Oliva E., 1994a, ApJ 429, 602
Moorwood A.F.M., Finger G., Gemperlein H., 1994b, The Messenger 77, 8
Moorwood A.F.M., van der Werf P.P., Kotilainen J.K., Marconi A., Oliva E., 1996a, A&A 308, L1
Moorwood A.F.M., 1996b, Space Sci. Rev. 77, 303
Moorwood A.F.M., Lutz D., Oliva E., et al., 1996c, A&A 315, L109
Netzer H., Laor A., 1993, ApJ 404, L51
Oliva E., Salvati M., Moorwood A.F.M., Marconi A., 1994, A&A 288, 457
Oliva E., Origlia L., Kotilainen J.K., Moorwood A.F.M., 1995, A&A 301, 55
Oliva E., Marconi A., Cimatti A., di Serego Alighieri S., 1998, A&A 329, L21
Oliva E., Marconi A., Moorwood A.F.M., 1999a, A&A 342, 87
Oliva E., Origlia L., Maiolino R., Moorwood A.F.M., 1999b, A&A 350, 9
Persic M., Mariani S., Cappi M., et al., 1998, A&A 339, L33
Rice G.H., Lonsdale C.J., Soifer B.T., et al., 1988, ApJS 68, 91
Richstone D., Ajhar E.A., Bender R., et al., 1998, Nat 395, 14
Rieke G.H., Lebofsky M.J., Thompson R.I., et al., 1980, ApJ 238, 24
Risaliti G., Maiolino R., Salvati M., 1999, ApJ 522, 157
Rowan-Robinson M., Mann R.G., Oliver S.J., et al., 1997, MNRAS 298, 490
Sanders D.B., Mirabel I.F., 1996, ARA&A 34, 749
Schreier E.J., Marconi A., Axon D.J., et al., 1998, ApJ 499, L143 (Paper II)
Siebenmorgen R., Moorwood A., Freudling W., Kaeufl H.U., 1997, A&A 325, 450
Skinner C.J., Bergeron L.E., Daou D., 1998, In: Casertano S., et al. (eds.) HST Calibration Workshop. STScI, Baltimore, in press
Smail I., Ivison R.J., Blain A.W., 1997, ApJ, 490, L5
Storchi-Bergmann T., et al., 1999, MNRAS 304, 35
Trentham N., Blain A.W., Goldader J., 1999, MNRAS 305, 61
Voit, M., et al., 1997, HST Data Handbook. Vol. I, Version 3.0 STScI, Baltimore